Dual shear wave induced laser speckle contrast signal and the improvement in shear wave speed measurement

Sinan Li,[1] **Yi Cheng,**[1] **Robert J Eckersley,**[2] **Daniel S Elson,**[3,4] **and Meng-Xing Tang**[1,*]

[1]*Department of Bioengineering, Imperial College London, London, SW7 2AZ, UK*
[2]*Department of Biomedical Engineering, King's College London, London, SE1 7EH, UK*
[3]*Department of Surgery and Cancer, Imperial College London, London, SW7 2AZ, UK*

[4]*daniel.elson@imperial.ac.uk*

[*]*mengxing.tang@imperial.ac.uk*

Abstract: Shear wave speed is quantitatively related to tissue viscoelasticity. Previously we reported shear wave tracking at centimetre depths in a turbid optical medium using laser speckle contrast detection. Shear wave progression modulates displacement of optical scatterers and therefore modulates photon phase and changes the laser speckle patterns. Time-resolved charge-coupled device (CCD)-based speckle contrast analysis was used to track shear waves and measure the time-of-flight of shear waves for speed measurement. In this manuscript, we report a new observation of the laser speckle contrast difference signal for dual shear waves. A modulation of CCD speckle contrast difference was observed and simulation reproduces the modulation pattern, suggesting its origin. Both experimental and simulation results show that the dual shear wave approach generates an improved definition of temporal features in the time-of-flight optical signal and an improved signal to noise ratio with a standard deviation less than 50% that of individual shear waves. Results also show that dual shear waves can correct the bias of shear wave speed measurement caused by shear wave reflections from elastic boundaries.

© 2015 Optical Society of America

OCIS codes: (170.1065) Acousto-optics; (110.0113) Imaging through turbid media.

References and links

1. J. Bercoff, M. Tanter, M. Muller, and M.Fink, "The role of viscosity in the impulse diffraction field of elastic waves induced by the acoustic radiation force," IEEE. Trans. Ultrason. Ferroelectr. Freq. Control. **51**(11), 1523–1536 (2004).
2. Y. K. Mariappan, K. J. Glaser, and R. L. Ehman, "Magnetic resonance elastography: A review," Clin. Anat. **23**(5), 497–511 (2010).
3. R. K. Wang, D. D. Sampson, S. A. Boppart, and B. F. Kennedy, "Special section guest editorial: optical elastography and measurement of tissue biomechanics," J. Biomed. Opt. **18**(12), 121501 (2013).
4. B. F. Kennedy, R. A. Mclaughlin, H. M. Kennedy, L. Chin, A. Curatolo, A. Tien, B. B. Latham, C. M. Saunders, and D. D. Sampson, "Optical coherence micro-elastography: Mechanical-contrast imaging of tissue microstructure," Biomed. Opt. Express **5**(7), 2113–2124 (2014).

5. L. Chin, A. Curatolo, B. F. Kennedy, B. J. Doyle, P. R. T. Munro, R. A. McLaughlin and D. D. Sampson, "Analysis of image formation in optical coherence elastography using a multiphysics approach," Biomed. Opt. Express **5**(9), 2913–2930 (2014).

6. X. Liang, M. Orescanin, K. S. Toohey, M. F. Insana, and S. A. Boppart, "Acoustomotive optical coherence elastography for measuring material mechanical properties," Opt. Lett. **34**(19), 2894–2896(2009).

7. A. Ahmad, J. Kim, N. A. Sobh, N. D. Shemonski, and S. A. Boppart "Magnetomotive optical coherence elastography using magnetic particles to induce mechanical waves," Biomed. Opt. Express **5**(7), 2349–2361 (2014).

8. A. Nahas, M. Bauer, S. Roux, and A. C. Boccara, "3D static elastography at the micrometer scale using Full Field OCT," Biomed. Opt. Express **4**(10), 2138–2149 (2013).

9. W. Qi, R. Li, T. Ma, J. Li, K. Kirk Shung, Q. Zhou, and Z. Chen, "Resonant acoustic radiation force optical coherence elastography," Appl. Phys. Lett. **103**(10), 103704 (2013).

10. T. M. Nguyen, B. Arnal, S. Song, Z. Huang, R. K. Wang, and M. ODonnell, "Shear wave elastography using amplitude-modulated acoustic radiation force and phase-sensitive optical coherence tomography," J. Biomed. Opt. **20**(1), 016001 (2014).

11. C. Li, G. Guan, F. Zhang, G. Nabi, R. K. Wang, and Z. Huang, "Laser induced surface acoustic wave combined with phase sensitive optical coherence tomography for superficial tissue characterization: a solution for practical application," Biomed. Opt. Express **5**(5), 1403–1418 (2014).

12. C. Li, G. Guan, F. Zhang, S. Song, R. K. Wang, Z. Huang, and G. Nabi, "Quantitative elasticity measurement of urinary bladder wall using laser-induced surface acoustic waves," Biomed. Opt. Express **5**(12), 4313–4328 (2014).

13. C. Li, G. Guan, Y. Ling, Y. T. Hsu, S. Song, J. T. J. Huang, S. Lang, R. K. Wang, Z. Huang, and G. Nabi, "Detection and characterisation of biopsy tissue using quantitative optical coherence elastography (OCE) in men with suspected prostate cancer," Cancer. Lett. **357**(1), 121–128 (2015).

14. C. Kim, R. J. Zemp, and L. V.Wang, "Intense acoustic bursts as a signal-enhancement mechanism in ultrasound-modulated optical tomography," Opt. Lett. **31**(16), 2423–2425(2006).

15. R. J. Zemp, C. Kim, and L. V. Wang, "Ultrasound-modulated optical tomography with intense acoustic bursts," Appl. Opt. **46**(10), 1615–1623(2007).

16. E. Bossy, A. R. Funke, K. Daoudi, A.-C. Boccara, M. Tanter, and M. Fink, "Transient optoelastography in optically diffusive media," Appl. Phys. Lett. **90**(17), 174111 (2007).

17. K. Daoudi, A.-C. Boccara, and E. Bossy, "Detection and discrimination of optical absorption and shear stiffness at depth in tissue-mimicking phantoms by transient optoelastography," Appl. Phys. Lett. **94**(15), 154103 (2009).

18. R. Li, D. S. Elson, C. Dunsby, R. Eckersley, and M.-X. Tang, "Effects of acoustic radiation force and shear waves for absorption and stiffness sensing in ultrasound modulated optical tomography," Opt. Express. **19**(8), 7299–7311 (2011).

19. Y. Cheng, R. Li, S. Li, C. Dunsby, R. J. Eckersley, D. S. Elson, and M.-X. Tang, "Shear wave elasticity imaging based on acoustic radiation force and optical detection," Ultrasound. Med. Biol **38**(9), 1637–1645 (2012).

20. Y. Cheng, S. Li, R. J. Eckersley, D. S. Elson, and M.-X. Tang, "Viscosity measurement based on shear-wave laser speckle contrast analysis," J. Biomed. Opt. **18**(12), 121511 (2013).

21. S. Li, Y. Cheng, L. Song, R. J. Eckersley, D. S. Elson, and M.-X. Tang, "Tracking shear waves in turbid medium by light: theory, simulation, and experiment," Opt. Lett. **39**(6), 1597–1600 (2014).

22. H. J. van Staveren, C. J. M. Moes, J. van Marie, S. A. Prahl, and M. J. C. van Gemert, "Light scattering in lntralipid-10% in the wavelength range of 400-1100 nm," Appl. Optics. **30**(31), 4507–4514 (1991).

23. L. Wang, S. L. Jacques, and L. Zheng, "MCMLMonte Carlo modeling of light transport in multi-layered tissues," Comput. Meth. Prog. Bio. **47**(2), 131–146 (1995).

24. R. Zemp, S. Sakadi, and L. V. Wang, "Stochastic explanation of speckle contrast detection in ultrasound-modulated optical tomography," Phys. Rev. E. **73**(6), 061920 (2006).

25. A. J. Rosakis, O. Samudrala, and D. Coker, "Cracks faster than the shear wave speed," Science **284**(5418), 1337–1340 (1999).

26. J. Ritsema, H. J. v. Heijst, and J. H. Woodhouse, "Complex shear wave velocity structure imaged beneath Africa and Iceland," Science **286**(5446), 1925–1928 (1999).

1. Introduction

Recently, mechanical characterization of tissue has provided new information for clinical diagnosis, e.g. fibrosis, oedema and tumours are detectable with ultrasound [1] or MR [2] elastography. Optical elastography systems, such as optical coherence elastography incorporated with optical coherence tomography [3], inherently provide optical contrast in addition to mechanical contrast. The latest development in optical coherence elastography (OCE) include micro-scale compression OCE [4] and the associated multiphysics model developed to improve the precision of the strain measurement [5]; Acoustomotive - [6] and Magnetomotive - [7] dynamic

internal excitation OCE; 3D full-field OCE [8] and resonant acoustic radiation force OCE [9]; surface acoustic wave [10] and shear wave [11] quantitative OCE and their clinical applications [12, 13]. Acoustic radiation force (ARF) assisted ultrasound modulated optical tomography (UOT) may even improve the depth of the dual contrast (optical plus mechanical) sensing to centimetre depths [14–18]. Based on the ARF-assisted-UOT, Cheng et. al developed a method to quantitatively measure the elasticity [19] and viscosity [20] at 1.2 cm depth in an optically turbid medium by tracking ARF-generated shear wave propagation using laser speckle contrast analysis. A systemic description of the theory, simulation and experiment can be found in [21]. This work opened up the possibility of a dual-contrast imaging tool at a clinical useful depth.

However, laser speckle contrast detection of multiple shear waves and their interaction/interference has not been studied yet. On the other hand, many shear wave elastography modalities, e.g. the method in [19] tracking a single shear wave, suffer from inaccurate estimation of shear wave speed near elastic boundaries due to shear wave reflections. Also, despite being a highly sensitive method for shear wave tracking (sensible to tens of nanometres displacement at cm-depth [21]), tissue movement in vivo may cause a reduction of the signal-to-noise ratio (SNR) due to speckle decorrelation. This manuscript reports the observation of two counter-propagating shear wave interaction using laser speckle contrast detection and its improvement in shear wave speed measurement by reducing the above effects.

Fig. 1. Experimental set-up and the schematic path length (a) and time-of-flight (b) of shear waves. Green shows the simulated optical detection volume in cross-section (a) and longitudinal plane (b) of the phantom. In the Monte Carlo simulation, a 532 nm point-like laser beam was used as the light source.

2. Materials and method

2.1. Experiment set-up and materials

A schematic of the experimental set-up is shown in Fig. 1(a). Tissue mimicking phantoms with various stiffnesses were illuminated by a 532 nm laser. The speckle patterns were detected by a charge-coupled device (CCD) camera (QImaging Retiga EXi, 1.4 million pixels, 6.45 μm per pixel, 12 bit digital output), and an iris was used to control the speckle size to be matched with a CCD pixel. Speckle contrast is defined as $C = \sigma/\bar{I}$, where σ is the standard deviation of the speckle intensities and $\bar{I}$ is the mean speckle intensity. Using a polariser, the background speckle contrast ranged from 0.83 to 0.86 for the phantoms used in experiments.

Shear waves were generated by transient acoustic radiation forces delivered by 1 ms ultrasound bursts of 5 MHz central frequency located at O_1 to generate a single shear wave and at O_1 and O_2 simultaneously to generate two shear waves. These waves propagated towards the

optical detection volume defined as the region in the phantom through which the detected scattered light passed. A Monte Carlo simulation of the optical detection volume is shown in Fig. 1, in which the phantoms had an optical scattering coefficient of 30 cm^{-1} and an anisotropy coefficient of 0.8 [16, 17, 22] .

The generated shear waves modulate the optical scatterer displacements and therefore modulate the phase of the multiply-scattered light. The speckle contrast C changes over time t as a function of the shear wave amplitude and the photons probability density at each voxel within the optical detection volume. We used a time-resolved speckle contrast difference signal $\Delta C(t) = C_b(t) - C(t)$ for shear wave tracking, where $C_b(t)$ is the background speckle contrast without shear waves. A 1 ms CCD exposure time was used to achieve a good compromise between the SNR of laser speckle detection and the temporal resolution of shear wave tracking. $\Delta C(t)$ was sampled at 10 KHz by repeatedly generating shear waves and delaying the start of CCD exposure by various times. The time-to-peak in $\Delta C(t)$ indicates the time-of-flight of shear waves to the optical axis (e.g. the dash line in Fig. 1(a)). As shear waves were generated at a relatively large distance away from the optical axis (25 mm), a high ultrasound negative pressure of 5.8 MPa was used, unless otherwise noted, to ensure that a good SNR was obtained.

To measure local shear wave speed, the shear wave - or one of the dual shear waves - was generated at another site with a different distance to the laser axis (e.g. at O_1' in Fig. 1(a)). The averaged shear wave speed within the differential distance ΔL is calculated by $\bar{C}_s = \Delta L / \Delta t$, or $\bar{C}_s = \Delta L / 2 \Delta t'$, where Δt and $\Delta t'$ are the shift of the time-to-peaks in $\Delta C(t)$ for the single shear wave and the dual shear wave respectively. The relationship will not be affected by heterogeneities in the medium and it can be derived from the schematic path length (Fig. 1(a)) and time-of-flight (Fig. 1(b)) of shear waves with $t_1 = t_2$ and $t_1' = t_2'$. The resolution of the shear wave speed measurement is thus primarily determined by ΔL, which was varied from 1 mm to 3 mm in experiment to study the effect on the accuracy of speed measurement.

2.2. Phantom

Phantoms were made with 4.0% intralipid concentration by volume and 0.8%, 1.0% and 1.2% agar concentrations by weight to achieve physiologically realistic optical scattering properties and mechanical contrasts [22]. An inhomogeneous phantom was also made by a cuboid stiff inclusion of 1.2% agar, with a length of 12 mm in the measurement interested dimension and lengths same to the background (0.8% agar) in the other two dimensions (namely are the height and thickness of phantom). Shear waves were generated and detected at half of the thickness i.e. 12 mm depth. As phantoms were held by two Perspex sheets in the water tank, artificial shear wave reflections could be caused by the phantom-Perspex and phantom-water interfaces due to the large shear wave impedance mismatch.

2.3. Simulation

The theory and simulation of shear wave tracking with coherent light and speckle contrast detection are described in [21]. The interaction between shear waves and light is simulated by coupling the analytic shear wave solution [1] with the multiply scattered photon trajectories predicated by the Monte Carlo modelling [23]. While the laser was not focused in the experiment, a point-like laser source was used in simulation for simplicity. The simplification does not affect the results qualitatively since the light will be unfocused soon as it enters the object and will become well diffused at the measurement depth. The shear wave displacement at each scatterer is calculated over time, and the phase change of photons due to the shear wave displacement is computed. With a weak scattering and other assumptions described in [24], $E(t)E^*(t+\tau)$ is accumulated over the multiply scattered photon path, where $E(t)$ is the electric field of a single photon on a CCD pixel without consideration of polarisation for simplicity,

and the CCD speckle contrast could be calculated via the first and second statistics. In our simulation, the shear wave speed and shear viscosity were 3.3 m/s and 0.1 Pa·s respectively. Other parameters were same as that in [1, 21] due to the similarity of the phantoms and ultrasound excitation beam used.

3. Result

3.1. Dual shear wave signal

Figure 2 shows the $\Delta C(t)$ detected by the system for an individual shear wave and two counter-propagating shear waves. For a single shear wave, $\Delta C(t)$ increased when the shear wave approached the optical detection volume and then decreased when the shear wave propagated away. When two counter-propagating shear waves were generated, a modulation of $\Delta C(t)$ was observed. The modulation pattern (circles in Fig. 2) showed stronger signal amplitude and sharper peaks which can provide a more accurate time-to-peak estimation. Before using the dual shear wave signal for speed measurement, the origin of the modulation pattern was studied with a simulation study.
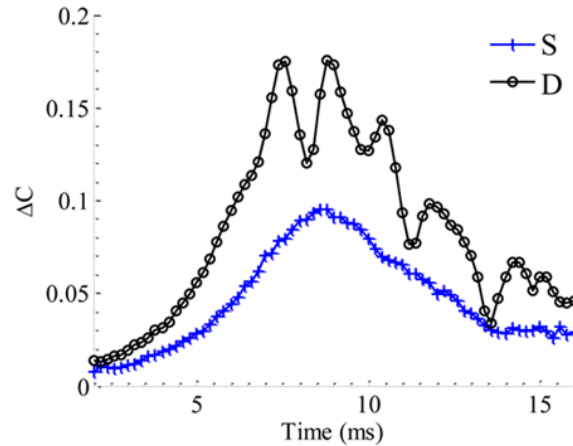
Fig. 2. $\Delta C(t)$ induced by the single shear wave (S) and the dual shear wave (D).

3.2. Simulation study

Without consideration of the aforementioned artificial shear wave reflections from the phantom boundaries, a simulation of the single shear wave - and dual shear wave - induced $\Delta C(t)$ is shown in Fig. 3 (solid lines). The dual shear wave signal formed two peaks at 7.3 ms and 8.4 ms, indicated by the arrows in Fig. 3(b). CCD speckle contrast is generally thought to be related with the velocity of scatterer movement. Figure 4 shows the normalised time-derivative of the shear wave displacement at 7.8 ms, 8.4 ms and 8.9 ms, corresponding to the two peak-time and the trough-time of the dual shear wave signal. Note that 0.5 ms was added onto the original peak/trough-times for a better representative of the collective effect during the 1 ms CCD exposure time. Figure 4 suggests that the peaks in $\Delta C(t)$ are formed when the velocity of dual shear wave displacements constructively interfere with each other near the centre of the optical detection volume, and the trough is formed when destructive interference occurred, which reduces both the scatterer velocity amplitude and the overlap between the shear waves and the optical detection volume.

The dashed lines in Fig. 3 show the simulation with consideration of shear wave reflections [21]. $\Delta C(t)$ becomes larger since the earliest reflected shear waves approach the optical
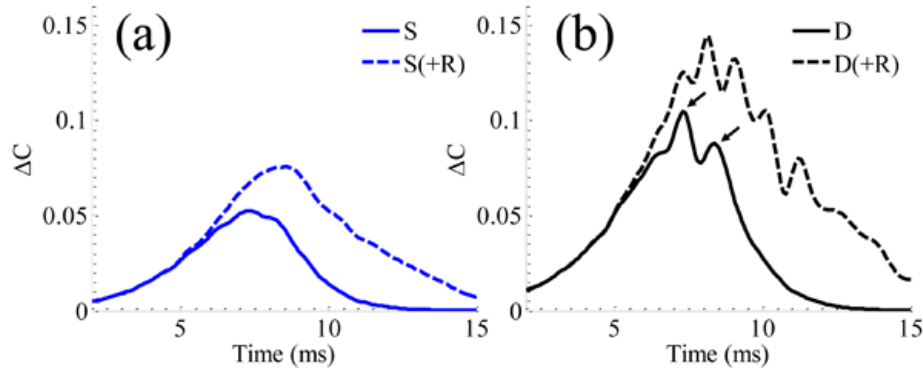
Fig. 3. Simulated $\Delta C(t)$ induced by single (S) and dual (D) shear wave with (+R) and without consideration of shear wave reflections.

detection volume and cause additional photon modulations. By comparing the dual shear wave simulation with and without shear wave reflections, the first peaks in Fig. 3(b) are observed to rightly correspond to 7.3 ms, suggesting that the first peak time should be used for estimation of shear wave time-of-flight as that is least affected by the shear wave reflections. The additional fluctuations after the second peak are due to the reflected shear waves alone, which could return from different sites on the boundaries to the optical detection volume.
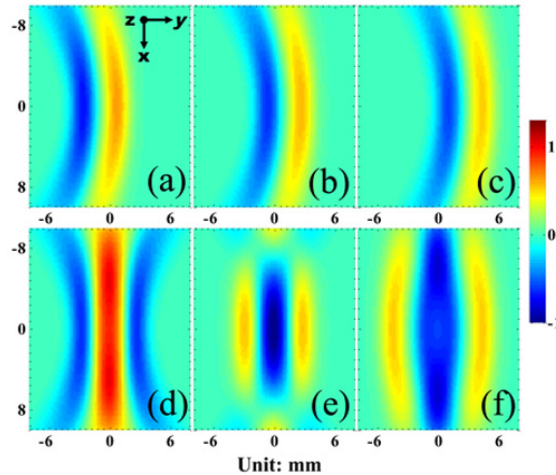
Fig. 4. Simulation of the normalised temporal derivative for single (a-c) and dual (d-f) shear wave displacement.

3.3. Time shift

To measure the experimental local shear wave speed, the generation site of one of the shear waves was translated from O_1 to O_1', with a differential distance $\Delta L = 2$ mm (Fig. 1(a)). Shifts of the peak time due to the differential distance are shown in Fig. 5, where the experimental data were fitted using smooth spline interpolation (solid lines). For the dual shear wave, the first peak was used for shear wave speed measurement. As in the theoretical prediction in Fig. 1, shift of the first peak time in dual shear wave signal was half that produced by the single shear wave (e.g. not generating shear wave at O_2).
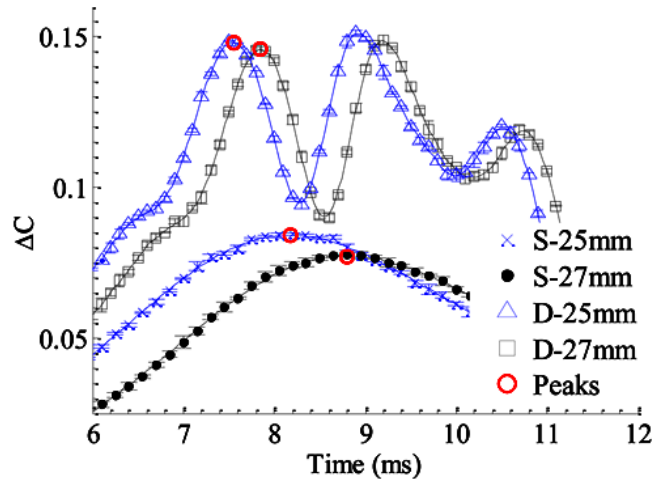
Fig. 5. Shift of peak time in $\Delta C(t)$ for single (S) and dual (D) shear waves in the experiment.

3.4. Shear wave speed measurement

Shear wave speed measurements using the single shear wave - and dual shear wave - approaches are shown in Fig. 6. The mean and standard deviation in the figure were produced by nine independent speed measurements from three repetitive $\Delta C(t)$ measurements. It shows that both the single shear wave and dual shear wave speed measurement had a good correspondence to the stiffness of phantoms (Fig. 6(a) - Fig. 6(c)). Also, given a fixed sampling rate of $\Delta C(t)$, e.g. 10 kHz used in the experiment, the accuracy of the shear wave speed measurement could be improved with an increased ΔL (therefore an increased Δt or $\Delta t'$) with a comprise of the spatial resolution of the shear wave speed measurement. In comparison, the dual shear waves speed measurement tends to be more accurate than the single shear wave result in terms of the standard deviation. This is because dual shear waves generated stronger shear wave amplitude and an improved definition of the temporal features (e.g. sharper peaks) in $\Delta C(t)$, which resulted in a higher SNR in the shear wave time-of-flight estimation.

Figure 6(d) shows the shear wave speed measurement on a stiff inclusion phantom. To demonstrate the good sensitivity of our system, the shear waves were generated at the same O_1/O_1' and O_2 but using an ultrasound negative pressure of 4.5 MPa at 5 MHz, equivalent to a mechanical index of 1.9 within the clinical ultrasound safety limit. The shear wave speed measured with single shear wave showed clear bias near the elasticity boundaries, e.g. speed was underestimated outside the inclusion and overestimated inside the inclusion. The biases were caused by the shear wave reflections from inclusion boundaries, but they were not observed in the dual shear wave speed measurement since the first peak time in the dual shear wave signal used for the time-of-flight estimation was not influenced by the shear wave reflections. The shear wave speed measurements in Fig. 6 agree with the previous report [19].

For a further illustration, Fig. 7 shows the peak time of shear waves originating from different scanning positions on the inclusion phantom. The peak times were smoothed and the difference in the vertical axis indicates the change of time-of-flight of shear wave due to the 2 mm ΔL. From the figure we can see that the peak time of the single shear wave signal was prolonged near inclusion boundaries, while the peak time of dual shear wave signal was very little affected by the shear wave reflections.
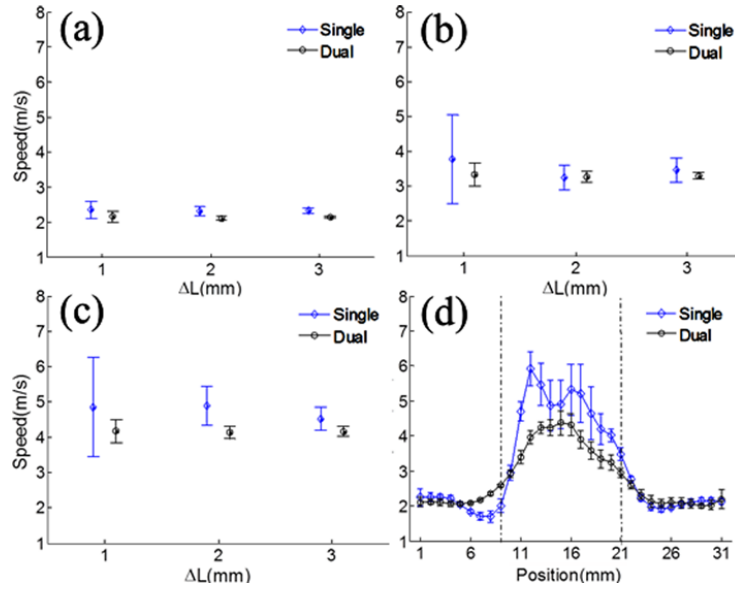
Fig. 6. Shear wave speed measured on 0.8% (a), 1.0% (b), 1.2% (c) and 0.8%-1.2% stiff inclusion (d) agar phantom. The dash lines indicate the inclusion boundaries.
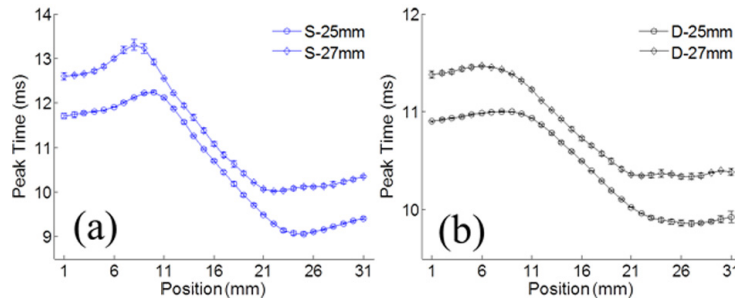

Fig. 7. Peak times of single (S) and dual (D) shear wave induced $\Delta C(t)$ at various inclusion phantom scan positions.

4.   Discussion

One may note that the shear wave speed measured with single shear wave is generally slightly higher than the dual shear wave measurements in Fig. 6. This may be caused by an overestimation of shear wave speed using the single shear wave approach due to the influence on the peak time estimation by the aforementioned artificial shear wave reflections from the phantom-Perspex and phantom-water interfaces (as predicted by Fig. 3(a)). When the shear wave reflection contributes to $\Delta C(t)$, the measured Δt always corresponds to a differential distance smaller than the actual horizontally translated ΔL because difference of the path length for reflected shear wave is always smaller than that of the original shear wave. Therefore using the known ΔL for speed calculation would result in an overestimation of the shear wave speed. The overestimation was consistent with our previous result, where the elasticity modulus evaluated by the single shear wave method was generally slightly larger than the independent mechanical compression test [19]. The dual shear wave approach should not suffer from this problem as the shear wave reflection will not bias the first peak time estimation as predicted by the Fig. 3(b).

The method can be applied to shear wave elastography. In practice, speckle decorrelation occurs in vivo. While speckle decorrelation should not affect the time-of-flight measurement (time-to-peak estimation of $\Delta C(t)$), it can reduce the signal-to-noise of $\Delta C(t)$. Since the dual shear wave approach creates an improved $\Delta C(t)$ intensity, a shorter CCD exposure may be used (e.g. 0.5 ms) to reduce the speckle decorrelation effect. In addition, measurements could be cardiac-gated to suppress any time-dependent speckle decorrelation due to pulsations. In Fig. 5, 50 sequential CCD exposures were used for the shear wave tracking. Thanks to the improved definition of the temporal features (sharper peaks) in $\Delta C(t)$, the number of exposures can be reduced using the dual shear wave modulation signal (e.g. 10 exposures during 7-8 ms are enough for the time-to-peak measurement with a prior estimation), and the total measurement time could be arranged within a few milliseconds using a fast CCD camera.

The compactness of the dual shear wave modulation pattern may have a dependence on the geometry and mechanical properties of the medium: for a stiff tissue with a fast shear wave speed, the separation of the peaks will be reduced and thus may need a higher $\Delta C(t)$ sampling rate. However, a faster shear wave speed may generate a further improved definition of the temporal features (even sharper peaks) in $\Delta C(t)$. This counter-effect on shear wave speed measurement will be evaluated, together with changing other parameters such as the viscosity and optical scattering of the medium. Compared with optical coherence elastography, the resolution of the approach is limited to mm scale depending on the differential distance selected. However, the laser speckle contrast detection method can achieve an imaging depth that is an order of magnitude larger than other optical methods. A future work is to evaluate the approach in tissue samples, where the 532 nm laser will be replaced by a near-infrared laser source to achieve an improved light penetration depth in tissues, and the dual shear waves will be generated nearer to each other using an ultrasound array to further improve the signal intensity. In addition, the dual shear wave approach should be explored by arranging the optical detection in a reflection mode. This dual shear wave approach could potentially be applied to applications other than biomedical ones, e.g. in material science for non-destructive evaluation [25] and in geology where shear wave propagation has been well studied for understanding the structure of upwellings in mantle [26]. The detection methods can also be expanded to other electromagnetic waves or ultrasound.

5.   Conclusion

In summary, we reported an observation of shear wave interference using laser speckle contrast detection. A temporal modulation of the speckle contrast difference was produced by two counter-propagating shear waves and the origin was suggested by simulation as an interference phenomenon between the velocity fields of dual shear wave displacement. Dual shear waves were shown to improve the shear wave speed measurement in terms of both accuracy and suppression of the boundary effect.

Acknowledgments